

Fabrication and characterization of on-chip silicon nitride microdisk integrated with colloidal quantum dots

Weiqliang Xie,^{1,2,*} Yunpeng Zhu,^{1,2} Tangi Aubert,^{2,3} Zeger Hens,^{2,3} Edouard Brainis,^{2,3} and Dries Van Thourhout^{1,2}

¹Photonics Research Group, Department of Information Technology, Ghent University-IMEC, Gent B-9000, Belgium

²Center for Nano and Biophotonics, Ghent University, B-9000 Ghent, Belgium

³Physics and Chemistry of Nanostructures, Ghent University, B-9000 Ghent, Belgium
weiliang.xie@intec.ugent.be

Abstract: We designed and fabricated free-standing, waveguide-coupled silicon nitride microdisks hybridly integrated with embedded colloidal quantum dots. An efficient coupling of quantum dot emission to resonant disk modes and eventually to the access waveguides is demonstrated. The amount of light coupled out to the access waveguide can be tuned by controlling its dimensions and offset with the disk edge. These devices open up new opportunities for both on-chip silicon nitride integrated photonics and novel optoelectronic devices with quantum dots.

©2015 Optical Society of America

OCIS codes: (130.3120) Integrated optics devices; (130.3130) Integrated optics materials; (140.3945) Microcavities; (160.4236) Nanomaterials.

References and links

1. E. S. Hosseini, S. Yegnanarayanan, A. H. Atabaki, M. Soltani, and A. Adibi, "High quality planar silicon nitride microdisk resonators for integrated photonics in the visible wavelength range," *Opt. Express* **17**(17), 14543–14551 (2009).
2. M. Ghulinyan, R. Guider, G. Pucker, and L. Pavesi, "Monolithic whispering-gallery mode resonators with vertically coupled integrated bus waveguides," *IEEE Photonics Technol. Lett.* **23**(16), 1166–1168 (2011).
3. Q. Li, A. A. Eftekhari, M. Sodagar, Z. Xia, A. H. Atabaki, and A. Adibi, "Vertical integration of high-Q silicon nitride microresonators into silicon-on-insulator platform," *Opt. Express* **21**(15), 18236–18248 (2013).
4. S. Romero-García, F. Merget, F. Zhong, H. Finkelstein, and J. Witzens, "Silicon nitride CMOS-compatible platform for integrated photonics applications at visible wavelengths," *Opt. Express* **21**(12), 14036–14046 (2013).
5. A. Z. Subramanian, P. Neutens, A. Dhakal, R. Jansen, T. Claes, X. Rottenberg, F. Peyskens, S. Selvaraja, P. Helin, B. Du Bois, K. Leysens, S. Severi, P. Deshpande, R. Baets, and P. Van Dorpe, "Low-loss singlemode PECVD silicon nitride photonic wire waveguides for 532–900 nm wavelength window fabricated within a CMOS pilot line," *IEEE Photonics J.* **5**(6), 2202809 (2013).
6. M. Eichenfield, R. Camacho, J. Chan, K. J. Vahala, and O. Painter, "A picogram- and nanometre-scale photonic-crystal optomechanical cavity," *Nature* **459**(7246), 550–555 (2009).
7. D. J. Moss, R. Morandotti, A. L. Gaeta, and M. Lipson, "New CMOS-compatible platforms based on silicon nitride and Hydex for nonlinear optics," *Nat. Photonics* **7**(8), 597–607 (2013).
8. X. Tu, J. Song, T. Y. Liow, M. K. Park, J. Q. Yiying, J. S. Kee, M. Yu, and G. Q. Lo, "Thermal independent silicon-nitride slot waveguide biosensor with high sensitivity," *Opt. Express* **20**(3), 2640–2648 (2012).
9. A. Dhakal, A. Z. Subramanian, P. Wuytens, F. Peyskens, N. Le Thomas, and R. Baets, "Evanescent excitation and collection of spontaneous Raman spectra using silicon nitride nanophotonic waveguides," *Opt. Lett.* **39**(13), 4025–4028 (2014).
10. A. Quattieri, F. Pisanello, M. Grande, T. Stomeo, L. Martiradonna, G. Epifani, A. Fiore, A. Passaseo, and M. De Vittorio, "Emission control of colloidal nanocrystals embedded in Si₃N₄ photonic crystal H1 nanocavities," *Microelectron. Eng.* **87**(5–8), 1435–1438 (2010).
11. S. Gupta and E. Waks, "Spontaneous emission enhancement and saturable absorption of colloidal quantum dots coupled to photonic crystal cavity," *Opt. Express* **21**(24), 29612–29619 (2013).
12. B. De Geyter, K. Komorowska, E. Brainis, P. Emplit, P. Geiregat, A. Hassinen, Z. Hens, and D. Van Thourhout, "From fabrication to mode mapping in silicon nitride microdisks with embedded colloidal quantum dots," *Appl. Phys. Lett.* **101**(16), 161101 (2012).
13. W. Xie, Y. Zhu, T. Aubert, S. Verstuyft, Z. Hens, and D. Van Thourhout, "Low-loss silicon nitride waveguide hybridly integrated with colloidal quantum dots," *Opt. Express* **23**(9), 12152–12160 (2015).

14. W. Xie, Y. Zhu, T. Aubert, Z. Hens, E. Brainis, and D. Van Thourhout, "On-chip hybrid integration of silicon nitride microdisk with colloidal quantum dots," 2015 IEEE International Conference on Group IV Photonics, 159–160 (2015).
 15. A. F. Oskooi, D. Roundy, M. Ibanescu, P. Bermel, J. D. Joannopoulos, and S. G. Johnson, "MEEP: A flexible free-software package for electromagnetic simulations by the FDTD method," *Comput. Phys. Commun.* **181**(3), 687–702 (2010).
 16. M. Cirillo, T. Aubert, R. Gomes, R. Van Deun, P. Emplit, A. Biermann, H. Lange, C. Thomsen, E. Brainis, and Z. Hens, "'Flash' synthesis of CdSe/CdS core-shell quantum dots," *Chem. Mater.* **26**(2), 1154–1160 (2014).
 17. W. Xie and D. Van Thourhout, "Fabrication of high-Q Silicon nitride microdisk resonator coupled with on-chip waveguide," *Proceedings Symposium IEEE Photonics Society Benelux*, 145–148 (2014).
-

1. Introduction

Silicon nitride (SiN), due to its fairly high optical index (~ 2.0), broad operating wavelength range, and compatibility with complementary metal-oxide-semiconductor (CMOS) processing technology, is a promising material as the basis for an integrated optics platform [1–5]. Various applications, such as optomechanics [6], nonlinear optics [7] and on-chip biosensing [8,9] have SiN photonic building blocks. Because of its dielectric nature however it is hard to realize active devices within the SiN platform and therefore efforts to bring optoelectronic functionality into the currently passive-only SiN platforms are of high scientific and technological interest. Particularly relevant is to combine gain materials directly with SiN building blocks such as waveguides and resonators for making optically active devices – e.g. a laser or a single photon emitter. As a class of such new materials, colloidal quantum dots (QDs) possess rich and adjustable optical and electrical properties, for instance, widely tunable emission spectra, and thus are suited well for the integration with passive SiN waveguides and cavities. This will enable studies of the interaction between QDs and electromagnetic radiation in a more controlled way and potentially trigger significant interest in fundamental studies and applications such as cavity-quantum electrodynamics, low-threshold lasers, and on-chip quantum emitters. The integration process should preserve the optical properties of the QDs and at the same time allow realizing high performance SiN circuits. More importantly, the integrating process should enable embedding QDs in a SiN environment to ensure both long-term stability for material properties and high spatial overlap between these emitters and the optical modes of a waveguide or cavity. From a practical viewpoint, it is also important that the active SiN-QD devices should be coupled with on-chip passive waveguides, allowing to combine multiple devices or to couple light in and out of devices. In fact, colloidal QDs have already been integrated with various types of passive SiN building blocks, including photonic crystal nanocavities [10,11] and micro-resonators [12]. In all these demonstrations, the QDs were integrated in an individual component and often experimental results show either weak coupling of QD emission into optical modes or low out coupling efficiency, because either they lack an effective embedding scheme or they lack an efficient coupling scheme. Recently, we have demonstrated a low-loss hybrid SiN-QD platform using integrated waveguide wires [13] and also reported preliminary results on the integration of QDs with SiN disks [14].

In the current paper, we provide in depth characterization results and according analysis of free-standing SiN microdisks vertically coupled with on-chip SiN bus waveguides and show the ability of controlling this coupling accurately. A layer of colloidal QDs was embedded inside the SiN disks, while the bus waveguides are free of QDs and hence exhibit low loss. Efficient coupling of QD photoluminescence (PL) to disk modes and eventually to the on-chip waveguides is experimentally realized. Furthermore, the tunability of coupling between disk and bus waveguide through changing geometrical parameters of the design, is demonstrated in both experiments and simulations. These active disks exhibit both a high quality (Q) factor and a large free spectral range (FSR), making them suitable for further development of on-chip laser sources. The developed approach is also relevant for the study of SiN cavities integrated with a few or a single QD for both fundamental studies and the realization of on-chip single photon emitters. Therefore the presented optically active devices open up new opportunities for the development of novel on-chip optoelectronic devices based on SiN photonics and QDs.

2. Design and fabrication

2.1 Design of free-standing SiN microdisk vertically coupled with on-chip waveguide

The proposed configuration for the SiN disk vertically coupled to an access waveguide is schematically shown in Fig. 1(a). The substrate is a silicon wafer with a 3 μm thermal SiO₂ layer. The bus waveguide is planarized with a SiO₂ cladding layer. The top SiN disk with the embedded QD layer at the center is suspended on an amorphous Si (aSi) pillar, with an sufficiently large undercut distance d (~ 3 μm) for preventing leakage loss of the fundamental transverse electric (TE) whispering gallery modes (WGM) to the aSi pillar. To tune the coupling strength, the horizontal offset, defined as the relative distance between waveguide center and the edge of the disk, is varied from -400 nm to $+400$ nm as schematically depicted in Fig. 1(a). From finite-difference time-domain simulations (FDTD), using a freely available software package [15], we adopt a height of ~ 125 nm for the bus waveguide, guaranteeing single TE mode operation at a wavelength of ~ 625 nm, the central emission wavelength of the QDs employed. The total disk height, including the top and bottom SiN layer and the QD layer was set to ~ 170 nm to ensure low loss for the fundamental TE WGM modes. Both the diameter of the SiN disk and the width of the bus waveguide are varied to investigate their effects on the disk-waveguide coupling and on the coupling of QD emission into disk modes. In Fig. 1(b), we present the simulated cross-sectional field profiles of the radial component (E_r) and intensity ($|E|^2$) for the fundamental TE mode in a suspended SiN disk with a 7 μm diameter. It is obvious that the field is well centered in SiN layer, ensuring maximum coupling with the QDs. Note also that the suspended configuration makes the mode is strongly confined in the disk, implying significantly reduced leakage loss to the substrate. More quantitatively, we simulated the Q-factor as function of the gap between disk and substrate for a mode at around 625 nm in the disk with a 7 μm diameter, as shown in Fig. 1(c). It can be seen that the substrate has a distinct influence on the Q-factor of the mode. For instance, with only a 150nm gap a Q factor of 1.3×10^4 is obtained, seven times as large as that for a disk directly fabricated on a SiO₂ substrate ($Q = 1.8 \times 10^3$). This shows that the vertical coupling configuration allows realizing waveguide-coupled free-standing disks with small diameters while supporting high Q WGM modes, or in other words allows large FSR and small modal volume, essential characteristics in many potential applications. In our design, the vertical gap was fixed at ~ 200 nm to facilitate coupling of the WGM modes to the underneath waveguide. An additional advantage of the vertical coupling scheme is that the fabrication steps for waveguide and disk are separated so that it is straightforward to integrate the QDs locally inside the disk and not in the access waveguides. This offers two distinct benefits: achieving low-loss passive connecting circuits and preventing undesired background signal from QDs elsewhere – critical requirements particularly in the context of low-light studies like controlled photon emitters. Realizing this in a lateral coupling scheme would be considerably more complex.

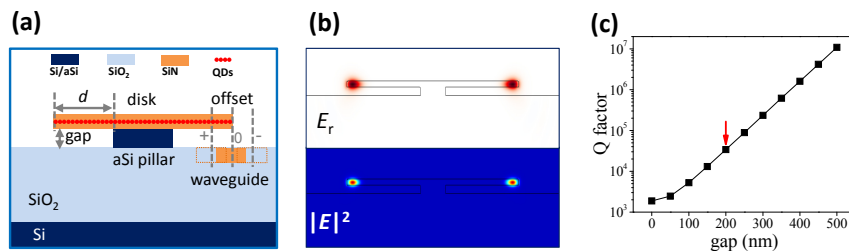


Fig. 1. (a) Cross-sectional view of SiN disk with embedded QDs vertically coupled with on-chip waveguide. (b) Simulated cross-sectional field profiles of radial component (E_r) and intensity ($|E|^2$) for the fundamental TE mode in suspended disk with a 7 μm diameter. (c) Simulated Q factor (mode wavelength ~ 625 nm) as a function of coupling gap for a 7 μm diameter disk with 170nm thickness. The red arrow indicates the gap of 200 nm used in our devices.

2.2 Fabrication of waveguide-coupled free-standing SiN microdisk with embedded QDs

In Figs. 2(a)-2(h), we schematically show the fabrication flow of the designed device. Firstly, a 125 nm thick SiN film is deposited onto a wafer with a 3 μm thermal SiO₂ box layer by using optimized plasma enhanced chemical vapor deposition (PECVD) process performed at a temperature of 270°C. The measured loss at ~ 630 nm for strip SiN waveguide is 1.16dB/cm, indicating a low material loss. Then the bus waveguide is patterned using optimized contact lithography and reactive ion etching (RIE) to form a strip waveguide that supports only a single TE mode at the designed wavelength, as shown in Fig. 2(a). This ensures only the TE WGM modes in the disk will be coupled out efficiently. The waveguide is then planarized by depositing a ~ 800 nm PECVD SiO₂ cladding and flattening the surface down to the top of the bus waveguide via optimized chemical mechanical planarization (CMP) process, as shown in Figs. 2(b) and 2(c). Next, a ~ 200 nm thick PECVD aSi layer is deposited to define the vertical coupling gap. Then the SiN-QD composite layer is deposited and patterned as depicted in Figs. 2(d) and 2(e). The SiN-QD stacked layer is prepared by successively depositing a ~ 80 nm bottom SiN, spin-coating a layer of QDs, and depositing ~ 80 nm top SiN for embedding the QDs. To define the disks a specifically optimized etching process [13] is used to obtain smooth and steep sidewalls. The QDs employed in our device are ~ 10 nm CdSe/CdS core/shell dots prepared according to the “flash” synthesis procedure [16], with a peak PL wavelength around 625 nm. For suspending the disk an alkaline based wet etching step is used. Since this process to some extent can also etch the QDs, an extra protection layer is patterned over the disks to prevent damaging the QDs as shown in Fig. 2(f). We used the commercially available ProTEK[®] B3, designed to withstand alkaline solutions, for this purpose. Finally the disk is undercut and the protective layer is removed to realize a free-standing SiN disk supported on an aSi pedestal as drawn in Figs. 2(g) and 2(h).

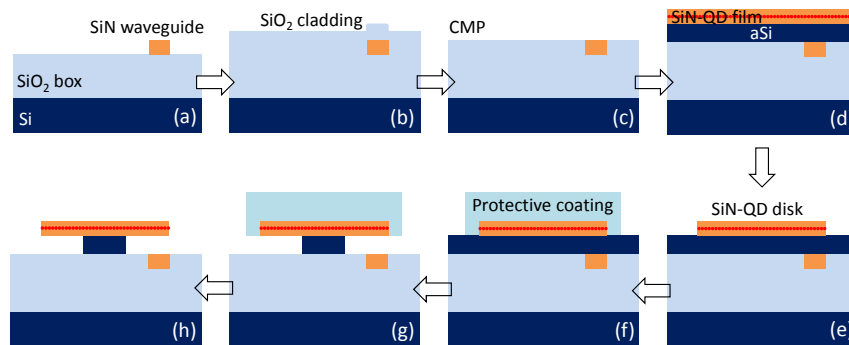


Fig. 2. Schematics of SiN-QD hybrid device fabrication flow. (a) Definition of SiN waveguide. (b, c) SiO₂ cladding deposition and CMP Planarization. (d, e) Deposition of aSi gap layer and SiN-QD-SiN films, and definition of SiN-QD disk. (f) Coating and patterning of protective layer. (g, h) Undercut etching of aSi and cleaning of protective layer.

In Fig. 3(a), we show optical images of fabricated devices with various disk diameters from 7 μm to 20 μm . It is clearly seen that the presently developed approach is capable of realizing on-chip free-standing SiN disk integrated with QDs. In Fig. 3(b), we show the scanning electron microscope (SEM) images of a fabricated device with a 7 μm diameter disk suspended on an aSi pillar with a ~ 3.0 μm undercut distance, under which the bus SiN waveguide is clearly buried in an oxide matrix for on-chip coupling. To check the morphology of the embedded QD layer, we made a focused ion beam (FIB) cross-sectional image along the dashed red line in Fig. 3(b) under the protection of a platinum (Pt) layer deposited in situ by electron beam and ion beam, shown in Fig. 3(c). The ~ 10 nm thick QD layer is perfectly embedded between the two layers of SiN and the SiN-QDs disk is supported on an aSi layer as expected. In Fig. 3(d), we show the tilted view of the enlarged disk sidewall area as indicated with dashed red box in Fig. 3(b) and the sidewall shows a continuously co-

etched surface for the composite layers without steps at the interfaces of the different layers, which is an important feature for high quality microdisk resonators.

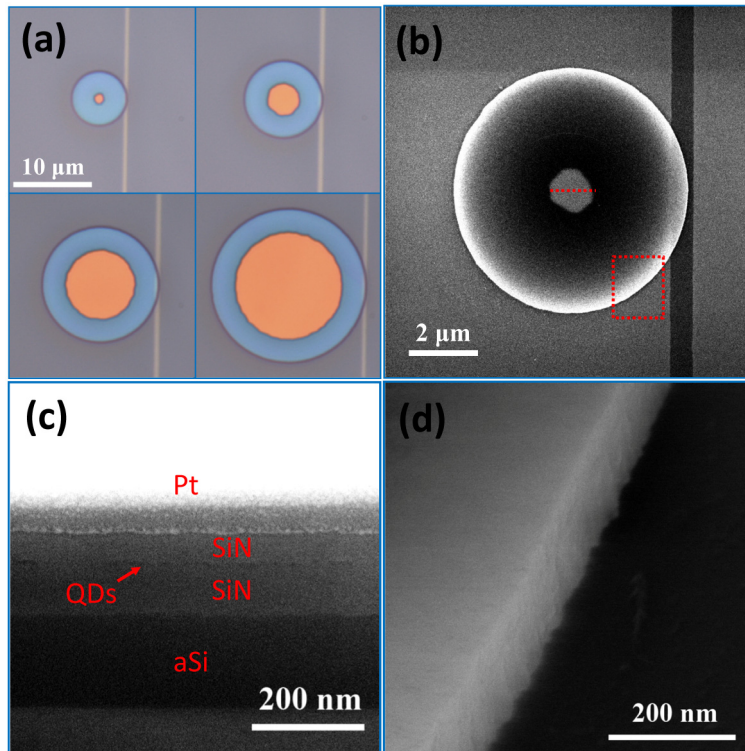


Fig. 3. (a) A set of optical images of fabricated devices with different disk diameters. All images have the same scale bar of $10\ \mu\text{m}$ as shown in the first left-top image. (b) SEM image of a device with a $7\ \mu\text{m}$ diameter disk. (c) FIB cross-sectional image of the disk taken along the dashed red line in (b). (d) SEM image of the tilted view of the disk sidewall area indicated with dashed red box in (b).

3. Characterization and discussion

3.1 PL characterization for SiN-QD disks with various diameters

To characterize the PL spectrum of the fabricated devices, we pumped the disks from the top using a 400 nm laser and collected the PL-signal from the cleaved facet of the bus waveguide using microlensed fibers. In Figs. 4(a) and 4(b), we show the normalized PL spectra of disks with two different diameters coupled to a $\sim 500\ \text{nm}$ wide bus waveguide with an about $-160\ \text{nm}$ offset, as defined in Fig. 1(a). The spectra clearly show that the QD emission is successfully coupled to the disk WGM. Taking advantage of the fact that the 500nm waveguide bus waveguide is in cut-off for the TM polarized modes, we only couple out the TE-like WGM modes of the disk. For the smallest disk of $7\ \mu\text{m}$ diameter, only the fundamental (i.e., 1st order) TE mode family is recorded in the spectrum shown in Fig. 4(a). This is in agreement with FDTD simulations showing that the higher order modes are lossy and exhibit a low Q-factor in this small disk. When increasing the diameter of the disk, a second family of WGM starts appearing, as shown in Fig. 4(b) for the $15\ \mu\text{m}$ disk. This family exhibits a larger FSR and through simulation we can identify it as originating from the radially second order TE-mode. In the insets of Figs. 4(a) and 4(b), we also denote the Q-factors of the modes around 622 nm determined by fitting a Lorentzian function. We obtain a Q of 1160 with a FSR of $\sim 8.9\ \text{nm}$ for the $7\ \mu\text{m}$ diameter disk and a Q of 4460 with a $\sim 4.15\ \text{nm}$ FSR for the $15\ \mu\text{m}$ diameter disk. Note that characterization of the modes with Q above

~4000 as shown in the fitting is already limited by the 0.05 nm resolution of the spectrometer we used. Another impressive signature of these spectra is that the background PL signal is very strongly suppressed, leading to sharp shoulders between the modes. This can be attributed to two factors – the enhanced interaction between the QD emission and the disk modes and the efficient coupling of the disk modes to the access waveguide. For photonic devices integrated with optical emitters, the background PL typically stems from emission directly radiated to free space (radiation modes) and light coupled to undesired modes, e.g. with an unwanted polarization or mode number. In our case, since the location of the thin QD layer almost perfectly overlaps with the maximum field intensity of the WGM modes in the disk, the proportion of QD emission coupled to these disk modes is significantly enhanced compared to that coupled to free space. Second, for collecting the PL we use the single-TE mode bus waveguide, which can efficiently couple out TE modes from the disk while coupling of any other modes as well as any scattered light is strongly suppressed. As a result, the PL spectra exhibit a very low background. For comparison, in the second inset of Fig. 4(b), we show the PL spectrum as collected on top of the disk. This spectrum is dominated by the broad background PL of the QDs and only a few of the WGM, as indicated by the red arrows are vaguely visible. Similar spectra reported in previous work [10,12] show that this background is unavoidable in free-space collection.

The envelope in the PL spectra in Figs. 4(a) and 4(b) can arise from the wavelength-dependent emission of the QDs itself but also from the wavelength-dependent disk-waveguide coupling strength. We believe the first effect actually plays the primary role. To verify this we prepared a SiN-QD-SiN slab waveguide using the similar process as depicted in Fig. 2. In Fig. 4(c) we show the PL spectrum of this slab waveguide together with that of the original QD solution. It can be seen that these spectra match well with the envelope of the device spectra in Figs. 4(a) and 4(b). Nevertheless, it should be mentioned that the wavelength-dependent coupling coefficient in the vertical coupling scheme cannot be neglected under some circumstances, for instance, when changing the coupling offset, we also observe a considerable shift in the PL spectra envelopes (not shown here). It is also important to note that, although the absolute intensity may decrease [12], the PL spectra of the QDs after embedding them in the SiN stack exhibits almost the same peak position and overall profile as the original PL spectra of the QDs in solution.

In Fig. 4(d), we plot the Q-factor and FSR for devices with various disk diameters but a constant bus waveguide width of ~500 nm and offset of -160 nm (measured around ~622 nm). A highest Q of 5740 and a FSR of 3.15 nm is achieved in the 20 μm diameter disk, an impressive result for such an active cavity. For the smallest disk, we attain a FSR of 8.9 nm and a moderate Q of 1160 (up to Q~1800 for some devices), promising for single-mode and low-threshold QD-based lasers on chip. The quality of the devices can still be improved by further optimizing the fabrication process, to attain a more uniform QD layer and smoother sidewalls, both factors reducing the scattering loss. We also present the simulated FSR values for different diameters in Fig. 4(d). In the simulation we assumed the disks were fabricated from a uniform SiN-layer with refractive index of 1.94 and thickness of 170 nm. The gap was fixed at 200 nm. The simulated results show good agreement with the measured values, with a discrepancy less than 4%, which can be attributed to small variation of the refractive index and dimensional and structural deviations between the designed and actually fabricated devices.

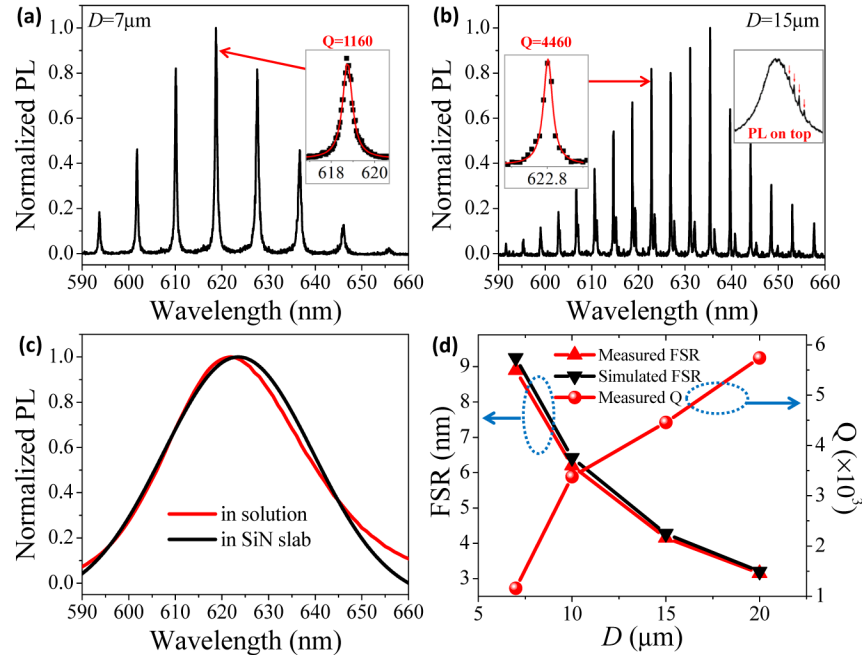


Fig. 4. (a, b) Normalized PL spectra of the devices coupled to ~ 500 nm wide waveguides with an offset of -160 nm, for disk diameters of 7 and 15 μm , respectively. The insets at the right side of (a) and left side of (b) show the fitted Q factors for representative fundamental WGM modes as denoted by the red arrows. The right-side inset in (b) shows the PL spectrum collected on top of the disk for comparison. (c) PL spectra of QDs in solution and in SiN slab. (d) Measured and simulated FSR values and fitted Q factors for different diameter (D) disks. For a fair comparison, both FSR and Q are calculated for the modes around ~ 622 nm, and Q factors are measured for the devices with ~ 500 nm waveguide width and -160 nm offset.

3.2 Tunability on the coupling strength of disk PL to bus waveguide

In a vertical coupling configuration, since the mode centers for different modes are spatially separated along the radial direction, the coupling coefficients for one family of modes can be tuned relatively to those of a different order by changing the offset between the bus waveguide and the disk or by adjusting the width of the bus waveguide. In fact, this tunability has already been studied in passive SiN disks [2,3,17]. In active devices it is of practical importance, e.g. to control the external efficiency of lasers. To investigate this further, we fabricated devices with varying offsets as well as varying bus waveguide widths. In Figs. 5(a) and (b), we show PL spectra of devices with a disk diameter of 10 μm and a 500 nm wide bus waveguide, having an offset of -60 nm and -160 nm, respectively. The spectra were not normalized and care was taken to take the experimental conditions constant so the absolute value of the recorded intensity can be compared between both configurations. When moving the bus waveguide away from the disk edge (i.e., reducing the offset to -160 nm), obviously the PL spectra evolve from a strong to a relatively weak coupling regime, with the overall light intensity coupled out decreasing by ~ 2.4 times. At the same time the Q-factor for the central peak is increasing by ~ 2 times. The possibility to efficiently and accurately tune the coupling strength comes from the strongly offset dependent coupling coefficient and is another advantage of the presented vertical coupling scheme. In Fig. 5(c), we also show the simulated offset-dependent power coupling efficiency (η) between the fundamental TE waveguide mode and the fundamental TE WGM modes in the disk with a diameter of 10 μm . Note that the parameter settings in the simulation are taken from the actually fabricated devices. With changing the offset from -60 to -160 nm, η decreases from 2.4% to 0.8% as

indicated by the red arrows in Fig. 5(c), which can account for the decrease of the out-coupled PL intensity in Figs. 5(a) and 5(b).

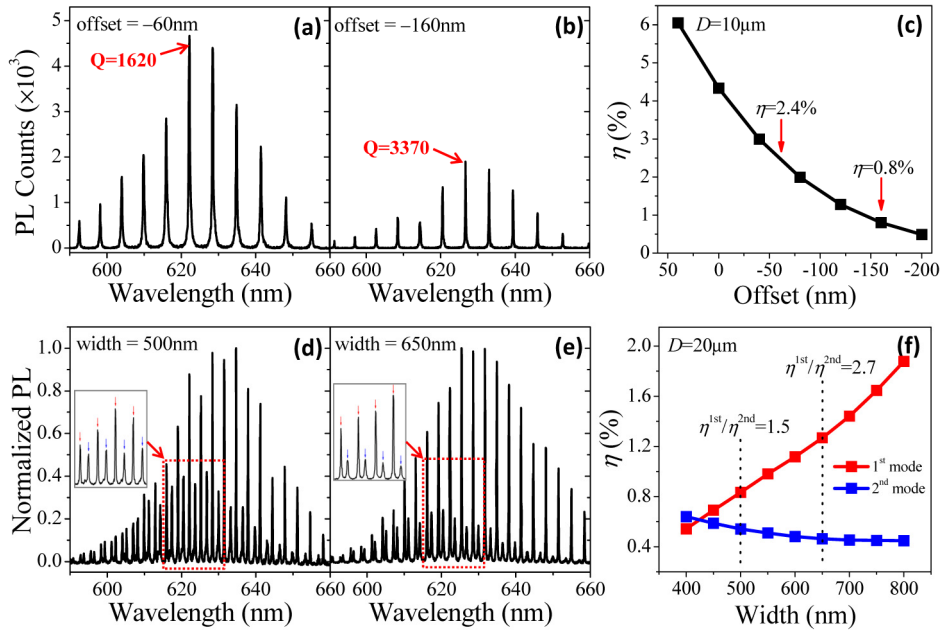


Fig. 5. (a, b) PL intensity spectra of the devices with a disk diameter of 10 μm and a 500 nm wide bus waveguide but under different offsets of -60 nm and -160 nm, respectively, together with Q-factors for the central peaks denoted by the red arrows. (c) The simulated offset-dependent coupling efficiency (η) between fundamental the TE waveguide mode and the fundamental TE WGM modes in the disk with a diameter of 10 μm . (d, e) Normalized PL spectra of the devices with a disk diameter of 20 μm and an offset of -160 nm but under different bus waveguide widths of 500 nm and 650nm, respectively. The insets show the zoom-in spectra for the selected regions as indicated with the red-dashed boxes. The red and blue arrows in the insets designate the 1st and 2nd order mode families, respectively. (f) The simulated waveguide width-dependent coupling efficiency between fundamental TE waveguide mode and 1st and 2nd order TE WGM modes in the disk with a diameter of 20 μm .

Instead of changing the offset, we can also modify the width of the bus waveguide to adjust the degree of coupling between different order disk modes and the bus waveguide. In Figs. 5(d) and 5(e), we show the PL spectra of devices with a disk diameter of 20 μm and an offset of -160 nm, coupled respectively to a 500 nm and 650nm bus waveguide. In this case the PL spectra were normalized to compare the change of coupling ratio of different order modes. The 20 μm diameter disk supports also radially higher order TE modes and these can be coupled out to the bus waveguide with considerable efficiency as clearly shown in Fig. 5(d). From their FSR, we can designate the two sets of modes as the radially 1st and 2nd order mode families as denoted by the red and blue arrows for a fraction of the spectrum in the insets of Figs. 5(d) and 5(e). By widening the bus waveguide, coupling of the 1st order modes can be enhanced with respect to the 2nd order modes as clearly illustrated in the inset of Fig. 5(e), for example, the PL intensity ratio of the 1st to 2nd order modes increases from 1.84 to 6.25 for the modes nearby 625 nm. The reduced coupling for 2nd order modes towards the wider waveguide can be explained by the fact that the fundamental mode in this wider waveguide is more strongly confined, reducing the overlap between this waveguide mode and the 2nd order disk modes, resulting in a rather weak coupling for these modes. The maximum electrical field of the 1st order modes on the other hand is located closer to the edge of disk, which ensures the spatial overlap with the waveguide mode remains substantial. From the simulated η for the 1st and 2nd order modes shown in Fig. 5(f), it is indeed obvious that widening the waveguide width from 400 nm to 800 nm the coupling strength for the 2nd

order modes decreases while it increases for the 1st order modes, leading to an enhanced coupling ratio of the 1st to 2nd order modes consistent with the measured results in Figs. 5(d) and 5(e). Finally, off course also adapting the gap between the free-standing disk and the waveguide offers an additional degree of freedom in engineering coupling efficiency as well as Q factor. The demonstrated tunability of coupling efficiency and cavity Q-factor could potentially be employed in further development of light sources, for example, in laser devices for tuning such parameters as threshold, line-width, and mode control.

4. Conclusion

In this paper, we designed and fabricated free-standing SiN microdisks hybridly integrated with embedded colloidal QDs, with those disks coupled to an on-chip access waveguide in a vertical coupling scheme. A hybrid integration platform built on an existing SiN photonic integrated circuits platform has been successfully demonstrated, enabling realizing on-chip QD-based active SiN building blocks. The detailed PL characterization of the fabricated devices has revealed both high performance – high quality factors together with large free spectral ranges – and an efficient coupling of QD emission to disk resonance modes and eventually to the on-chip waveguide. Furthermore, by changing geometrical parameters associated with the proposed vertical configuration, the coupling between the disk whispering gallery modes and the bus waveguide could be efficiently and accurately tuned. The presented optically active devices provide new opportunities not only for the on-chip SiN photonics community but also for the development of novel optoelectronic devices based on QDs.

Acknowledgment

The authors acknowledge the ERC-ULPPIC, H2020-MSCA phonsi, and the IAP Photonics@be projects for financial support.